NJC

PAPER

View Article Online
View Journal | View Issue

Cite this: *New J. Chem.*, 2016, **40**, 4236

SAPO-34 templated by dipropylamine and diisopropylamine: synthesis and catalytic performance in the methanol to olefin (MTO) reaction†

Dong Fan,[ab] Peng Tian,*[a] Shutao Xu,[a] Dehua Wang,[ab] Yue Yang,[a] Jinzhe Li,[a] Quanyi Wang,[a] Miao Yang[a] and Zhongmin Liu*[ac]

Received (in Montpellier, France) 2nd September 2015,
Accepted 13th January 2016

DOI: 10.1039/c5nj02351c

www.rsc.org/njc

In this work, a comprehensive study of the hydrothermal synthesis and catalytic performance of SAPO-34 templated by the isomeric dipropylamine (DPA) and diisopropylamine (DIPA) was carried out. SAPO-34 with a faster crystallization rate and lower Si content could be obtained with DIPA as the template, suggesting the better templating efficacy of DIPA than DPA. Theoretical calculations reveal that DIPA possesses more favourable non-bonding interactions with the CHA framework and the electronic configuration is of vital importance in determining the template efficacy. SAPO-34-DIPA with low silicon contents exhibits excellent performance, over which a maximum selectivity of ethylene plus propylene (87.2%) is observed. This value should be among the top ever reported. The surface Si enrichment on the crystals, which is both template- and condition-dependent, is revealed to be of significant influence in the catalytic performance. The relatively homogenous Si distribution in the crystals, lower acid concentration and weaker acid strength corporately make SAPO-34-DIPA an excellent MTO catalyst.

1. Introduction

Silicoaluminophosphate (SAPO) molecular sieves are an important class of open-framework crystalline materials, which possess intrinsic cavities and channels and find widespread use in gas separation and catalysis.[1–3] Since their first invention by the Union Carbide scientists in the early 1980s,[4,5] a variety of SAPO molecular sieves with unique structures have been successfully synthesized.

The structures of SAPO molecular sieves cover a wide range of different framework types; some are analogous to certain aluminosilicate zeolites, while a lot have unique topologies with no zeolitic counterparts.[6] Among the various SAPOs, SAPO-34, the SAPO isomorph of zeolite chabazite, has been attracting special attention.[7–12] The CHA (IZA code) framework of SAPO-34 is fabricated by the ordered stacking of the double 6-rings (D6R, Fig. 1).[13,14] The resulting framework, characterized by the barrel-like CHA cages with 8-ring openings, is considered to be the ideal incubation cradle for the hydrocarbon pool

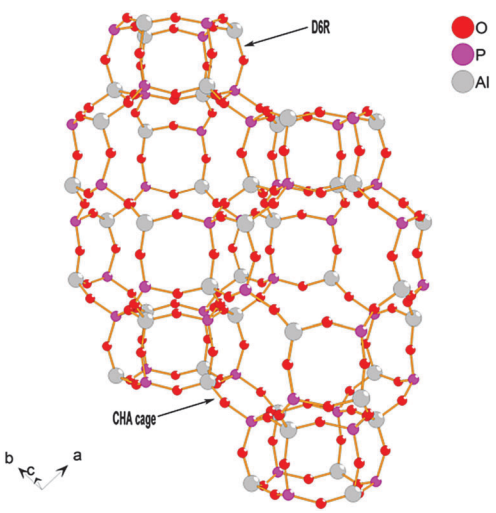

Fig. 1 The barrel-like cages of SAPO-34 (Si omitted); two CHA cages are shown in the structure.

[a] *National Engineering Laboratory for Methanol to Olefins, Dalian National Laboratory for Clean Energy, Dalian Institute of Chemical Physics, Chinese Academy of Sciences, Dalian 116023, China. E-mail: tianpeng@dicp.ac.cn, liuzm@dicp.ac.cn*

[b] *University of Chinese Academy of Sciences, Chinese Academy of Sciences, Beijing 100049, China*

[c] *State Key Laboratory of Catalysis, Dalian Institute of Chemical Physics, Chinese Academy of Sciences, Dalian 116023, China*

† Electronic supplementary information (ESI) available: Powder XRD patterns of the selected samples in Table 1, powder XRD patterns of the samples with shortened crystallization time, SEM images of the selected SAPO-34 samples, TG-DTG-DSC curves of the SAPO-34 samples templated by DPA and DIPA, ^{27}Al and ^{31}P MAS NMR of the selected SAPO-34 samples and a detailed tabular summary of the MTO catalytic performance of the investigate samples. See DOI: 10.1039/c5nj02351c

intermediates (active species) in the methanol to olefin (MTO) reaction.[15–19] In actual fact, SAPO-34 based catalysts have been successfully applied in a commercialized MTO utility with a production capacity of 600 000 tons of light olefins per annum.[20]

Till now, organic templates or structure directing agents (SDAs) are indispensable in the synthesis of SAPO molecular sieves, in spite of the development of multiple synthetic strategies, including the hydrothermal method,[19,21] the solvothermal method,[22] dry-gel conversion,[12,23] and solvent-free synthesis.[24] It is found that one template may produce molecular sieves with different structures by varying the synthetic conditions; and one type of molecular sieve could also be synthesized using different templates.[25] The elemental composition, local microscopic structure and morphology of one specific molecular sieve may change with the templates.[26–28] Therefore, the catalytic performance of the products may be different.

Research on the synthesis of SAPO-34 and its physicochemical/catalytic properties is one of the most interesting issues in the area of molecular sieves. Many amines have been claimed to be used as the template for the synthesis of SAPO-34.[29–32] The structure-directing ability varies among these organic amines, as indicated by the distinct crystallization rate, compositions range *etc.* Among the amines, two isomeric amines, DPA and DIPA arouse our great interest. Both amines have been extensively studied as the templates for SAPO-11, SAPO-31, and SAPO-41, but less attention has been paid to their structure-directing ability to the formation of SAPO-34.[33,34] Our recent work shows that DIPA could be an efficient SDA to direct the aminothermal synthesis of SAPO-34 with high solid yield and good MTO catalytic performance.[35] It would be therefore interesting to study the hydrothermal synthesis of SAPO-34 templated by DIPA and DPA and their physicochemical properties (catalytic behaviors). In addition, considering the closely related molecular structures of both amines, a theoretical study on their templating ability might also help us better understand the host–guest relationship and the role of organic amines in the synthesis of molecular sieves, which is of fundamental importance towards *a priori* or *de novo* synthesis.[25,36–40]

In this contribution, a comparative study of the hydrothermal synthesis of SAPO-34 using DPA and DIPA as the template is carried out. Theoretical calculations are performed to elucidate the different templating efficacy of two amines. The obtained SAPO-34 samples are characterized in detail and tested as catalysts for the MTO reaction. Distinct catalytic performance over samples is observed. Factors that might influence the catalytic properties are discussed. Fortunately, some enlightening results are discovered.

2. Experimental

2.1 Synthesis procedures

A typical hydrothermal synthesis procedure using DPA or DIPA as the template is as follows. Pseudoboehmite (70.0 wt%), water, phosphoric acid (85 wt%), and silica sol (30 wt%) were sequentially added into a plastic beaker. The resulting mixture was stirred at room temperature for 30 min to form a homogenous gel. After further addition of DPA or DIPA as the template, the mixture was transferred into a stainless steel autoclave and sealed quickly. Subsequently, the autoclave was transferred into an oven, heated to 200 °C and kept for a certain crystallization period under tumbling conditions. After the crystallization, the as-synthesized samples were obtained through combined processes of centrifugation, washing and drying at 373 K overnight.

The reference sample R1 was synthesized using triethylamine (TEA) as the template according to the same procedure mentioned above.

The solid yield of the samples was calculated by the following formula: yield (%) = $(M_{\text{sample}} \times 83\%) \times 100/(M_{Al_2O_3} + M_{P_2O_5} + M_{SiO_2})_{\text{gel}}$, where M_{sample} and $(M_{Al_2O_3} + M_{P_2O_5} + M_{SiO_2})_{\text{gel}}$ stand for the weight of as-synthesized solid samples and the dry mass of three inorganic oxides in the starting mixtures, respectively. The weight percentage of dry mass in the as-synthesized samples (83%, template and water removed) was derived from the TG analysis.

2.2 Characterization

The powder XRD patterns were recorded on a PANalytical X'Pert PRO X-ray diffractometer with CuKα radiation (λ = 1.54059 Å), operating at 40 kV and 40 mA. The chemical composition of the solid samples was determined using a Philips Magix-601 X-ray fluorescence (XRF) spectrometer. The crystal morphology was observed by scanning electron microscopy (SEM, KYKY-AMRAY-1000B). All the solid state NMR experiments were performed on a Bruker Avance III 600 spectrometer equipped with a 14.1 T wide-bore magnet. The resonance frequencies were 156.4, 242.9, 119.2, 150.9 and 600.1 MHz for ^{27}Al, ^{31}P, ^{29}Si, ^{13}C and ^{1}H, respectively. ^{27}Al, ^{31}P, ^{13}C and ^{1}H MAS NMR experiments were performed on a 4 mm MAS probe with a spinning rate of 12 kHz. ^{27}Al MAS NMR spectra were recorded using one pulse sequence. 200 scans were accumulated with a π/8 pulse width of 0.75 μs and a 2 s recycle delay. Chemical shifts were referenced to $(NH_4)Al(SO_4)_2{\cdot}12H_2O$ at −0.4 ppm. ^{31}P MAS NMR spectra were recorded using high-power proton decoupling. 32 scans were accumulated with a π/4 pulse width of 2.25 μs and a 10 s recycle delay. Chemical shifts were referenced to 85% H_3PO_4 at 0 ppm. ^{13}C MAS NMR spectra were recorded using high-power proton decoupling. 244 scans were accumulated with a π/2 pulse width of 5 μs and a 4 s recycle delay. Chemical shifts were referenced to admantane with the upfield methine peak at 29.5 ppm. ^{1}H MAS NMR spectra were recorded using one pulse program. 4 scans were accumulated with a π/2 pulse width of 4.4 μs and a 60 s recycle delay. Chemical shifts were referenced to admantane at 1.74 ppm. ^{29}Si MAS NMR spectra were recorded with a 7 mm MAS probe with a spinning rate of 6 kHz using high-power proton decoupling. 5000–6000 scans were accumulated with a π/4 pulse width of 2.5 μs and a 10 s recycle delay. Chemical shifts were referenced to 4,4-dimethyl-4-silapentane sulfonate sodium salt (DSS). Textural properties of the calcined samples were determined by N_2 adsorption at 77 K on a Micromeritics ASAP 2020 system. The total surface area was calculated using the BET equation. The micropore volume and micropore surface area were evaluated using the *t*-plot method. TG and DSC analysis was performed

on a Perkin-Elmer Pyris-1 TGA and DTA-7 analyzer with the temperature-programmed rate of 10 °C min^{-1} at an air flow rate of 100 ml min^{-1}. X-ray photoelectron spectroscopy (XPS) analysis was conducted on a VG ESCALAB MK2 XPS system. AlKα X-ray (1486.6 eV) radiation was used for exciting the photo electron spectra. A hemispherical analyzer was employed for electron detection, and the pass energy of the analyzer was set at 50 eV. Quantification analysis of the surface elemental compositions was determined by the areas of the core-level peaks of Si 2p, Al 2p and P 2p. The temperature-programmed desorption of ammonia (NH_3-TPD) experiments was conducted in a Micromeritics Autochem II 2920 device. 0.1 grams of the sample particles (40–60 mesh) were loaded into a U-quartz tube and pretreated at 650 °C for 60 min in a gas mixture of NH_3 and He flow to saturate the sample surface with NH_3 adsorption (60 min). After this, He flow was purged through the sample for 30 min to remove the weakly adsorbed NH_3 molecules. The measurement of the desorbed NH_3 was performed from 100 °C to 700 °C (10 °C min^{-1}) at a He flow rate (20 ml min^{-1}).

2.3 Calculation details

The host–guest interactions between the SAPO-34 framework and template molecules are theoretically studied based on molecular mechanics. All the calculations are carried out using the Material Studio 6.0 software provided by the Accelrys Inc. The conformations of the investigated templates and the interaction energies are described using the COMPASS force-field. A super cell comprised of 4 rhombohedra unit cells of the CHA structure is built to model the host framework of SAPO-34. Periodic boundary conditions are applied. The framework atoms are kept fixed during the calculations. The optimal docking positions of the organic molecules inside the host framework are determined *via* a simulated annealing process. The Ewald summation method is chosen for the calculation of the Coulombic electrostatic energy. For the van de Waals interaction energy, the atom-based summation method with a cutoff value set at 12.5 Å is applied.

2.4 Catalyst evaluation

The MTO reaction was carried out using a fixed-bed reactor at atmospheric pressure. 1.2 grams of calcined SAPO-34 crystals was loaded into the reactor. The catalyst was pretreated in a flow of nitrogen atmosphere at 823 K for 1 h. Nitrogen flow was turned off when the reactor was cooled down to 723 K. A mixture of methanol and water with a CH_3OH/H_2O weight ratio of 40/60 was consequently pumped into the reactor. The weight hourly space velocity (CH_3OH WHSV) was 4 h^{-1}. The products were analyzed by an Agilent GC7890 gas chromatograph equipped with a FID detector and an HP-PLOT Q capillary column.

The methanol conversion was defined as the percentage of CH_3OH consumed during the MTO reaction. The selectivity was defined as the weight percentage of each compound in the total products. It should be noted that dimethylether (DME) was considered as a reactant instead of product here.

3. Results and discussion

3.1 The influence of the synthetic parameters

Table 1 lists the overall results of the hydrothermal syntheses using both DPA and DIPA as the template. The powder XRD patterns of the selected samples are presented in Fig. S1 (ESI†). As can be seen, the crystallization of SAPO-34 is significantly affected by the silicon ratio in the initial gel for both amine systems. With DPA as the template, AlPO-11 having the AEL (IZA code) structure is obtained in the absence of silicon. Increasing the molar ratio of silicon to 0.3, SAPO-34 crystallizes with minor SAPO-11 as impurities. Pure SAPO-34 could only be obtained when the value is increased to as high as 0.5. A similar trend is observed for the samples synthesized using the DIPA template. With the increasing silicon content, a gradual phase transition from AEL to CHA is observed.

Another notable parameter that is found to exert great influence on the phase selectivity of the syntheses is the template dosage. In the DPA system, SAPO-31 is synthesized when the molar ratio of DPA in the initial gel equals to 1. Increasing the value to 3 or 5, SAPO-34 is readily formed in the pure phase, suggesting that higher DPA loading is favourable for the CHA phase selectivity. Similarly, a larger amount of DIPA template is also found to be a prerequisite for the synthesis of pure SAPO-34. This is in agreement with the previous reports that increasing the gel alkalinity is better for the formation of the pure phase of SAPO-34.

Despite the similar influential factors for SAPO-34 syntheses using DPA and DIPA templates mentioned above, some variances have also been observed. One variance lies in the different crystallization rates of SAPO-34. After a crystallization period of 3 hours, SAPO-34 is readily crystallized with high relative crystallinity in the DIPA system, while the amorphous phase still dominates the product with DPA as the template even after a crystallization duration of 12 h (Fig. S2, ESI†). This suggests the faster crystallization rate of SAPO-34 templated by DIPA. Another difference between the two systems comes from the

Table 1 Summary of the synthesis of SAPO molecular sieves using DPA or DIPA as the template

Sample[a]	R	Al_2O_3	P_2O_5	SiO_2	H_2O	Product	Yield (%)
1	1.0 DPA	1.2	0.9	0.5	40	SAPO-31	—
2	3.0 DPA	1.2	0.9	0.0	40	AlPO-11	—
3	3.0 DPA	1.2	0.9	0.3	40	SAPO-34 + minor SAPO-11	55.6
4	3.0 DPA	1.2	0.9	0.5	40	SAPO-34	74.0
5	3.0 DPA	1.2	0.9	0.75	40	SAPO-34	77.6
6	5.0 DPA	1.2	0.9	0.5	40	SAPO-34	80.4
7	1.0 DIPA	1.2	0.9	0.5	40	SAPO-11	—
8	3.0 DIPA	1.2	0.9	0.0	40	AlPO-11	—
9	3.0 DIPA	1.0	0.9	0.2	40	SAPO-34 + minor SAPO-11	90.6
10	3.0 DIPA	1.2	0.9	0.3	40	SAPO-34	83.1
11	3.0 DIPA	1.2	0.9	0.5	40	SAPO-34	84.5
12	3.0 DIPA	1.2	0.9	0.75	40	SAPO-34	85.2
R1	3.5 TEA	1.0	1.0	0.3	50	SAPO-34	70

[a] All the synthesis experiments are carried out at 200 °C for 48 h under tumbling conditions.

Table 2 Textural properties of the SAPO-34 samples templated by different amines

Sample	Surface area (m^2 g^{-1})			Pore volume (cm^3 g^{-1})	
	S_{total} [a]	S_{micro} [b]	S_{ext} [c]	V_{total}	V_{micro} [d]
4	592	589	3	0.29	0.28
10	605	600	5	0.30	0.28
R1	595	594	1	0.28	0.28

[a] BET surface area. [b] *t*-Plot micropore surface area. [c] *t*-Plot external surface area. [d] *t*-Plot micropore volume.

lowest silicon content requirement for the formation of the pure SAPO-34 phase. The syntheses under the DPA system are more sensitive to the silicon content in the initial gel, as is indicated by the difficulty for pure phase SAPO-34 synthesis when the molar ratio of silicon is less than 0.5 (sample 3). In effect, attempts to synthesize SAPO-34 with a lower silicon content have been extensively carried out by us using DPA as the template, but failed in vain with the inherent occurrence of the AEL phase as impurities. Moreover, the solid yields of SAPO-34 templated by DIPA are higher than those with DPA as the template, suggesting the better atomic utilization efficiency under the former system. This is interesting in view of the similar structure and alkalinity of both amines. It is inferred that the synthesis differences between DIPA and DPA systems might stem from the different template efficacy of the two isomers, which will be further discussed in the later part from a theoretical point of view.

Samples 4 and 10 synthesized using DPA and DIPA as the corresponding template respectively, are selected to undergo detailed characterization. SEM images reveal that both samples possess the typical rhombohedral morphology with sizes ranging from 2 to 5 μm (Fig. S3–S5, see ESI†). N_2 adsorption experiments reveal that the textural properties of the two samples are quite similar to each other, with a high micropore surface area around 600 m^2 g^{-1} and a large micropore volume of 0.28 cm^3 g^{-1} (Table 2). These values are also close to those of reference sample R1 synthesized with TEA as the template (Table 1). Both the SEM images and textural data verify the good crystallinity of the SAPO-34 samples.

3.2 Template status in the as-synthesized samples

The status of the templates inside the CHA frameworks of SAPO-34 is investigated by a combined analysis of TG-DSC experiments and multiple NMR techniques including ^{13}C and ^{1}H MAS NMR spectroscopy.

^{13}C MAS NMR spectra of the as-synthesized samples 4 and 10 are presented in Fig. 2. For sample 10 templated by DIPA, two resonance peaks centered around 49 and 19 ppm are observed, which could be explicitly assigned to the two different carbon positions (C_1 and C_2) of the DIPA molecule, respectively. As for sample 4, an extra peak at 11 ppm occurs, corresponding to the additional C_3 position in the DPA molecule. Both spectra are congruent with the standard ^{13}C spectra of DPA and DIPA molecules, suggesting their intactness inside the as-synthesized samples.[41]

The intactness of the two templates is further corroborated by the ^{1}H MAS NMR spectra (section B, Fig. 2). Three resonance peaks corresponding to the three different hydrogen positions (7.3, 3.5 and 1.3 ppm) are observed on sample 10, while four peaks (7.5, 3.0, 1.7 and 1.1 ppm) due to the presence of an additional H position in the DPA molecule are observed on sample 4. Another message inferred from the ^{1}H MAS NMR spectra is that the molecules of the two templates are in the protonated form. The chemical shifts of the two investigated samples show more resemblance to the standard spectra of diisopropylamine hydrochloride and dipropylamine hydrochloride. Due to protonation, the peaks corresponding to the H atoms in the imide groups are observed to shift to a lower magnet field comparing to the non-protonated form for both templates.[41] This conclusion is also confirmed by a quantitative analysis. The deconvoluted results reveal that the ratio of the

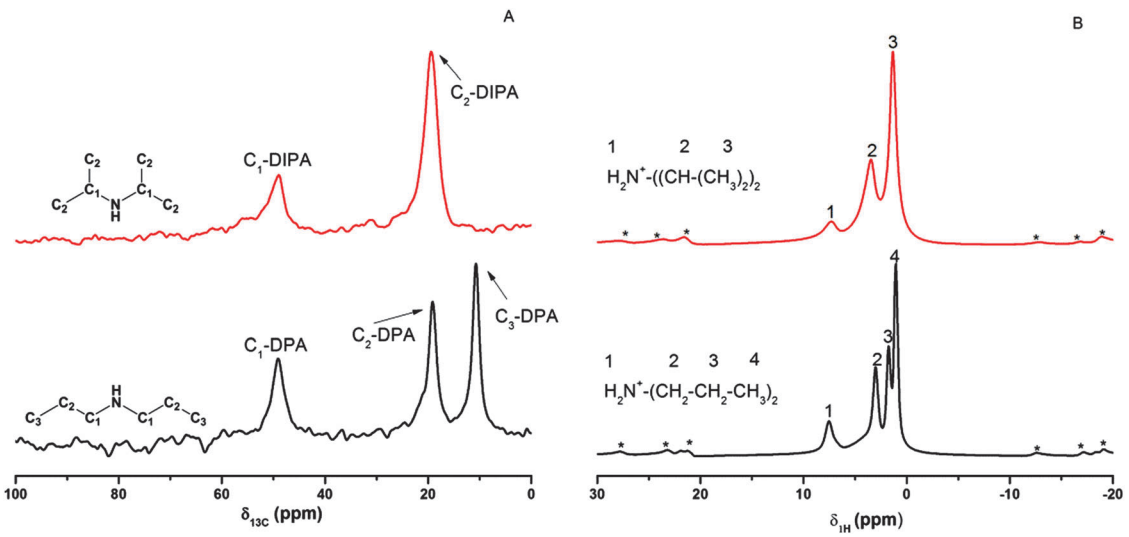

Fig. 2 ^{13}C MAS NMR (A) and ^{1}H MAS NMR (B) spectra of the as-synthesized samples 4 (below) and 10 (above); asterisks indicate spinning sidebands.

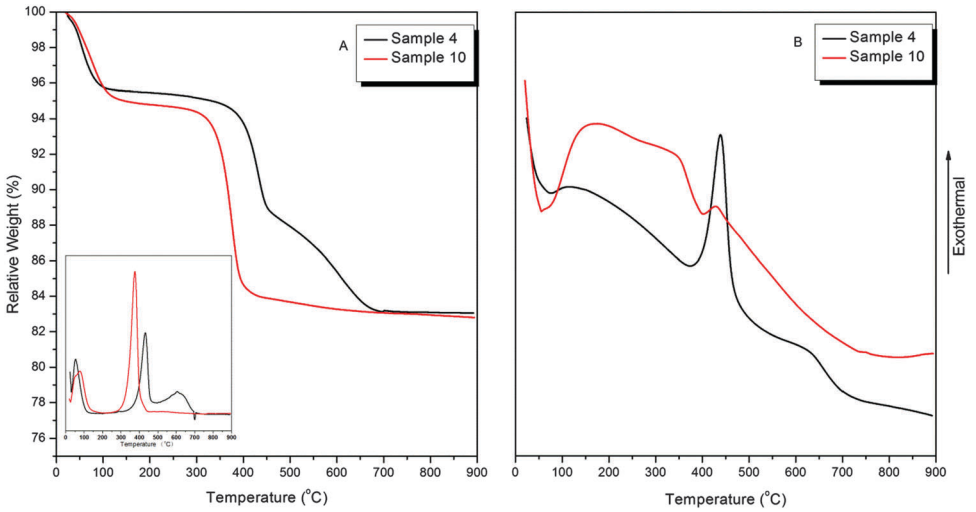

Fig. 3 TG (A) and DSC (B) curves of the as-synthesized samples of 4 and 10; the corresponding DTG curves of the two samples are also presented (inset, A).

H atoms bonding to nitrogen over total H atoms per molecule is about 1/7.8 and 1/8.1 for DPA and DIPA templates, respectively. Such high values unambiguously indicate that an extra proton is linked to the nitrogen atoms in both amines, despite the possibility that minor quantities of water might exist and cause a little underestimation of the calculation results.

TG and DSC curves of the as-synthesized samples 4 and 10 are presented in Fig. 3. The DTG curves are also shown in the inset. For sample 4 templated by DPA, a typical three-step weight loss is observed. The first weight loss ($T < 150$ °C) accompanied by the endothermic process is ascribed to water removal. The second weight loss (350–450 °C) with the strong exothermic peak is due to the preliminary combustion of the DPA molecules. The third weight loss (450–690 °C) is probably attributed to the further removal of the heavier organic residues in the channels and cages of SAPO-34. A three-step weight loss is also observed on sample 10. However, the third weight loss is not as obvious as that on sample 4. For sample 10, the combustion removal of the organic compounds is mainly completed in the second weight loss at a relatively lower temperature (<450 °C). It is speculated that some variances in the microstructure or silicon distribution (acid properties) might exist and have led to this interesting phenomenon. No obvious weight loss or heat flow change ascribing to framework collapse is observed till 900 °C for both samples, suggesting their good thermal stability. Notice that the weight losses ascribed to the template removal are essentially the same (about 12 wt%) for both samples. Based on the elemental compositions and topological structure of the samples, it is calculated that only one DPA or DIPA molecule is encapsulated in each CHA cage. This value equals to that of TEA or TEAOH reported previously.[28,30]

3.3 Theoretical simulations

The theoretical density and distribution of the template molecules is investigated through a simulated annealing process based on the Monte Carlo method.[42] A super cell comprised of 2 × 2 × 1 rhombohedra unit cells is built as the model frameworks, in order to give the template molecules more conformation freedom.[43] Note that the Si atoms are omitted here for the difficulty in determining their exact distributions. The negative framework charge caused by silicon substitution is instead simulated by a uniform background charge model,[44,45] by evenly distributing the charge among the framework Al and P atoms. The guest template molecules are supposed to be in a protonated form to balance the negative charge of the frameworks, which is also congruent with the ^{1}H MAS NMR analysis. COMPASS forcefield, a consistent force field with unified parameters for both inorganic and organic systems, is selected to describe all the interactions.[46,47] Simulation results reveal that only one molecule could be incorporated into each cage of the CHA framework for both DPA and DIPA. Higher loading of the templates, *e.g.* 5 DPA or DIPA molecules for each super cell, consistently leads to a simulation failure due to energy unconvergence. The theoretical density of the template derived from the simulation results is congruent with the experimental results. The optimal docking positions and geometries of the DPA and DIPA templates are presented in Fig. 4. All the template molecules are found to be located inside the CHA cages with relatively larger dimensions.

After determining the optimal distributions of the template molecules, further calculations to study the interactions between the isomeric templates and the CHA frameworks are carried out. We focus particularly on the non-bonding interaction energy, an energy term that has been extensively applied as the criterion to justify the template efficacy.[36,37,39,43,48] TEA, a common SAPO-34 template, is also considered and calculated here as reference. The calculated non-bonding energies and the two components of it, *i.e.* the van der Waals interaction and Coulomb electrostatic interaction energy, are listed in Table 3. As is demonstrated, DIPA possesses the strongest non-bonding interactions with the CHA framework. The non-bonding interaction energy is calculated to be −102.7 kcal mol^{-1}, a value much higher than

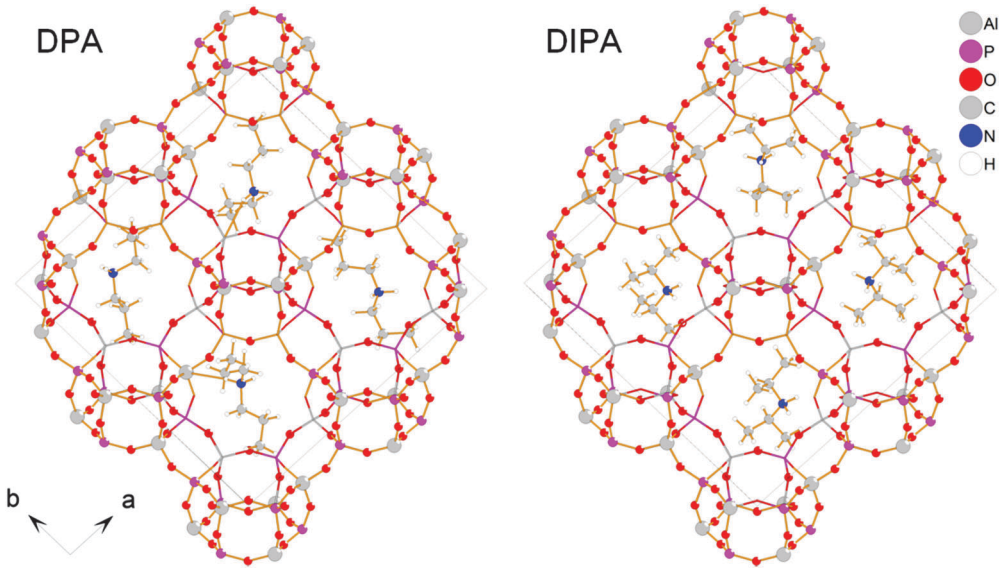

Fig. 4 Optimal distributions of DPA and DIPA molecules inside the CHA cages of SAPO-34 (viewed along the [001] direction).

that of DPA and the reference TEA template. It suggests that, among the three investigated organic amines, the DIPA template could stabilize the CHA frameworks with the highest efficiency. Accordingly, the template efficacy of DIPA for SAPO-34 synthesis is superior to that of both DPA and TEA, in good agreement with the experimental results shown in the previous section.

Further digging into the two comprising parts of the non-bonding energies, it could be found that the van der Waals interaction energies for the three templates are quite close to each other. The variation in the non-bonding interactions originates predominately from the Coulomb electrostatic interactions, suggesting that, compared with geometry fit, the electronic configurations are more significant in determining the template efficacy of the three investigated templates. This founding could well explain the difficulty of low-silicon SAPO-34 synthesis using the DPA template. It is inferred that more silicon species are required to be incorporated to create a relatively favourable host–guest electrostatic interaction between the CHA frameworks and the DPA molecules, and thus a much harsher limitation on Si content in the initial gel is observed for pure phase SAPO-34 synthesis in the DPA templating system. Interestingly, although it is previously reported that the omitting of the electrostatic interactions has little influence on the non-bonding energy trend, we demonstrate herein that the electrostatic interactions might do exert a significant effect on the non-bonding interactions and thus the template efficacy, at least in our investigated systems and calculation protocols.

Table 3 Calculated interaction energies (per template molecule) between the CHA frameworks and template molecules

Template[a]	Electrostatic	van der Waals	Non-bonding
DPA	−28.07	−22.31	−50.39
DIPA	−80.73	−21.97	−102.70
TEA	−44.19	−21.55	−65.74

[a] The unit of the above data is uniformly presented in kcal mol^{-1}.

3.4 Local atomic environments in the calcined samples: ^{27}Al, ^{31}P and ^{29}Si MAS NMR

The local atomic environments of three elements (Al, P and Si) in the calcined samples 4, 10 and R1 are investigated by MAS NMR experiments and the corresponding spectra are presented in Fig. S7, S8 (ESI†), and Fig. 5, respectively. As is shown in the ^{27}Al MAS NMR spectra (Fig. S7, ESI†), a single symmetrical peak centered at around 35 ppm is observed on all the three investigated samples, suggesting the sole existence of tetra-coordinated aluminum in the three calcined samples. Likewise, the ^{31}P MAS NMR spectra of the three samples (Fig. S8, ESI†) exhibit one symmetrical resonance signal around at −30 ppm, revealing that all phosphorous species exist in the form of the P (4Al) coordination environment. However, some coordination diversities are observed for the Si species. For samples 10 and R1, one strong resonance at around −94 ppm is observed, corresponding to the predominant Si(4Al) environment in both samples. In addition, a small shoulder peak at around −98 ppm could also be discerned in the spectrum of sample R1, which suggests the existence of Si(3Al) species. Sample 4, templated by DPA, possesses a much more complex silicon environment with the co-existence of several silicon coordination environments. This is reasonable considering its high silicon content in the bulk phase (Si/(Si + Al + P) = 0.122, see Table 4).

It is quite interesting to see the difference in the Si coordination environments of samples 10 and R1, considering their close Si content and the same template number per CHA cage. According to our previous research, the phenomenon is possibly related to the different Si distributions in the SAPO-34 crystals (from the core to the surface) of samples 10 and R1.[21,30,49] XPS experiments were hence carried out to investigate the surface elemental compositions of the two calcined samples and the results are shown in Table 4. Both samples exhibit a surface Si enrichment phenomenon, confirming the non-uniform distribution of Si in the crystals with an increase from the core to the surface.

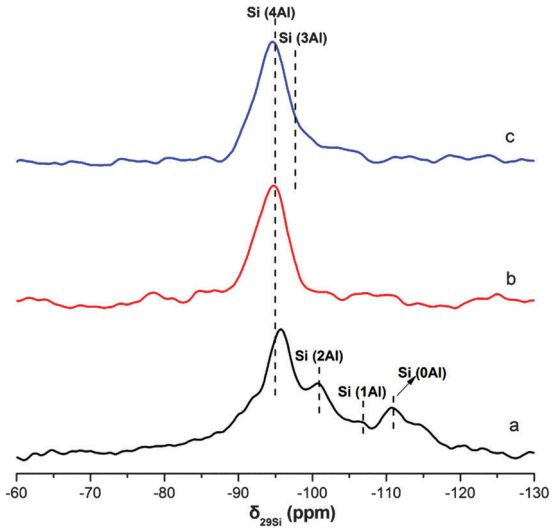

Fig. 5 ^{29}Si MAS NMR spectra of the calcined samples 4 (a), 10 (b) and R1 (c).

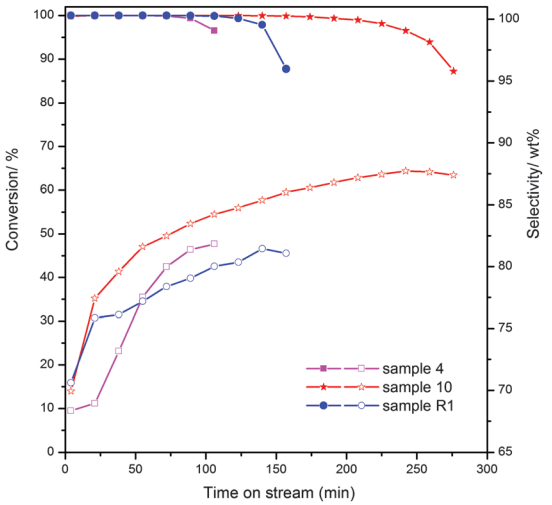

Fig. 6 Methanol conversion (solid) and (C_2H_4 + C_3H_6) selectivity (hollow) during the MTO reaction on samples 4, 10 and R1 (reaction conditions: 723 K, CH_3OH WHSV = 4 h^{-1}, 40 wt% methanol solution).

Table 4 The bulk and surface compositions of samples

Sample	XRF[a]	XPS[b]	R[c]
4	$Al_{0.496}P_{0.383}Si_{0.122}$	—	—
10	$Al_{0.504}P_{0.420}Si_{0.076}$	$Al_{0.484}P_{0.391}Si_{0.124}$	1.63
R1	$Al_{0.486}P_{0.434}Si_{0.080}$	$Al_{0.453}P_{0.341}Si_{0.206}$	2.58

[a] The bulk elemental compositions derived from XRF analysis. [b] The surface elemental compositions derived from XPS analysis. [c] The surface Si enrichment index R is defined as $[Si/(Si + P + Al)]_{surface}/[Si/(Si + P + Al)]_{bulk}$ to indicate the degree of surface enrichment degree of Si species.

The surface Si content of sample R1 could reach 0.206 (Si/(Si + Al + P)), which is obviously higher than that of sample 10 and consistent with the appearance of Si(3Al) species observed in the ^{29}Si spectrum of sample R1. It is speculated that the Si environments on the crystal surface of sample R1 should be more complex than those in the bulk phase. Other Si species such as Si(2Al), Si(1Al) and Si(0Al) might also exist, but pitifully could not be detected because of their relatively small quantity.

3.5 Catalytic performance in the MTO reaction

The MTO performance of the obtained SAPO-34 is investigated on a fixed-bed micro-reactor. The results are given in Fig. 6 and Table S1 (ESI†). Sample R1 templated by TEA are also evaluated as reference catalysts.

A poor MTO performance is observed on sample 4, which shows the shortest catalyst lifetime (89 min) and a low selectivity towards ethylene plus propylene (81.4%). This should be related to its high silicon content and complex silicon environments, considering the similar crystal sizes and textural properties of the investigated samples. According to the literature,[20,50] SAPO-34 with lower Si content (lower acidity), corresponding to the major existence of the Si(4Al) environment in the framework, generally exhibits better MTO reaction performance. It is thus reasonable to see that sample 10 with decreased silicon content exhibits good MTO results, whatever be the catalyst stability and the olefin selectivity. The selectivity of ethylene plus propylene rises with the time on stream and reaches a maximum of 87.2% at total methanol conversion. The corresponding catalyst lifetime is 208 min, much longer than that of sample 4. Notably, such a selectivity of ethylene plus propylene should be among the highest values ever reported for the MTO reaction, suggesting the excellent catalytic properties of sample 10 templated by DIPA.

The superiority of sample 10 as the MTO catalyst is further confirmed by comparing its catalytic performance with sample R1 possessing similar Si content to sample 10. The catalyst lifetime and selectivity of ethylene plus propylene on sample R1 are 123 min and 80.4%, respectively. The different catalytic performance of sample 10 and R1 might result from their different surface Si enrichment degree on the two samples. Weckhuysen *et al.*[51] once reported that MTO reaction initially occurred in the near-surface region of the HSAPO-34 crystal. The larger coke compound formed in the cages at the edges of the crystal would cause diffusion limitation and inhibit the release of the product generated inside. This implies that the Si coordination environment on the crystal surface of SAPO-34 has a very important effect on the MTO reaction. Therefore, it is inferred that the relatively low surface silicon amount together with the dominant Si(4Al) environment in sample 10 slows down the coke formation on the outer surface and benefit the olefin selectivity and catalyst lifetime.

NH_3-TPD experiments are further carried out to detect the acid properties of the samples. As illustrated in Fig. 7, two desorption peaks are observed for all three samples. The peaks centered at around 185 °C are ascribed to ammonia desorbed from the weak acid sites, while the peaks at higher temperatures correspond to the NH_3 desorption from the moderate/strong acid sites, which are mainly associated with the Brønsted acid sites and have close relationship with the MTO catalytic properties. Both the concentration and strength of the moderate/strong acidities in the three samples have the following order:

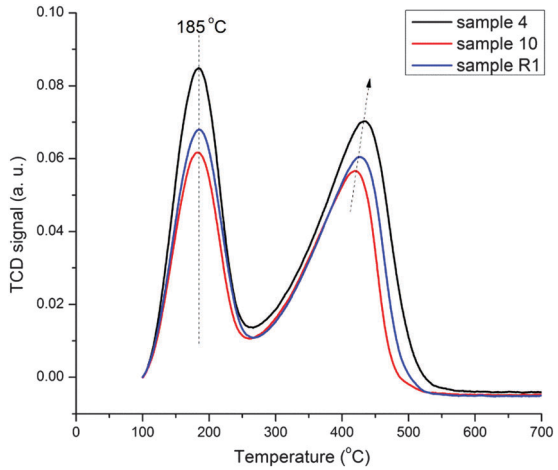

Fig. 7 Temperature programmed desorption curves of ammonia for the calcined samples 4, 10 and R1.

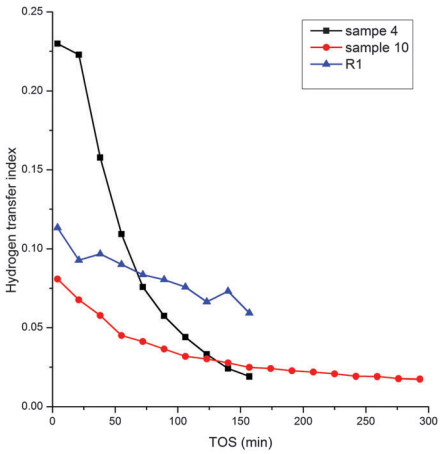

Fig. 8 Hydrogen transfer index (HTI, defined as C_3H_8/C_3H_6) of methanol conversion over the investigated catalysts.

sample 4 > sample R1 > sample 10. This is consistent with the ^{29}Si NMR spectra and XPS results, because the Si island (Si(nAl), n = 1–3) could generate stronger acidities compared to the Si(4Al) environment. Note that this order is in line with the hydrogen transfer index (Fig. 8) of the three samples, but opposite to the catalytic lifetime and the selectivity to ethylene plus propylene, confirming that the lower acidity concentration and relatively weaker acid strength are beneficial to the MTO reaction.

4. Conclusions

SAPO-34 has been hydrothermally synthesized using both dipropylamine (DPA) and diisopropylamine (DIPA) as the template. Synthetic results indicate that DIPA has better templating ability for the SAPO-34 synthesis than DPA. The different template efficacy of the two amines is rationalized *via* theoretical calculations based on molecular mechanics, which reveals the stronger non-bonding interactions of DIPA with the CHA framework. It is also found that the electronic configurations exert greater influence than the geometrical fit in determining the non-bonding interaction energy under our investigated systems. Most interestingly, the hydrothermally synthesized SAPO-34 using the DIPA template displays excellent methanol-to-olefin (MTO) catalytic performance with a long lifetime and high olefin selectivity (87.2%), which should be among the highest values ever reported for the MTO reaction. Further characterization reveals that the relatively low surface Si enrichment, lower acidity concentration and weaker acid strength associated with the DIPA template led to this encouraging result. The higher solid yield and excellent MTO performance might help the hydrothermal synthesis of SAPO-34 using the DIPA template find its applications industrially.

Acknowledgements

The authors would like to acknowledge the National Natural Science Foundation of China (Grant no. 21476228, Grant no. 21473182 and Grant no. 21506207) for the support of this project. Dong Fan would also like to acknowledge the generous financial support of DNL-Topsøe scholarship provided by Haldor Topsøe Corporation.

Notes and references

1 M. E. Davis, *Nature*, 2002, **417**, 813–821.
2 Z. Wang, J. Yu and R. Xu, *Chem. Soc. Rev.*, 2012, **41**, 1729–1741.
3 J. Yu and R. Xu, *Chem. Soc. Rev.*, 2006, **35**, 593–604.
4 B. M. Lok, C. A. Messina, R. L. Patton, R. T. Gajek, T. R. Cannan and E. M. Flanigen, *J. Am. Chem. Soc.*, 1984, **106**, 6092–6093.
5 S. T. Wilson, B. M. Lok, C. A. Messina, T. R. Cannan and E. M. Flanigen, *J. Am. Chem. Soc.*, 1982, **104**, 1146–1147.
6 C. Baerlocher and L. B. McCusker, Database of Zeolite Structures, http://www.iza-structure.org/databases/, accessed February 26, 2014.
7 Ø. B. Vistad, D. E. Akporiaye and K. P. Lillerud, *J. Phys. Chem. B*, 2001, **105**, 12437–12447.
8 O. B. Vistad, D. E. Akporiaye, F. Taulelle and K. P. Lillerud, *Chem. Mater.*, 2003, **15**, 1639–1649.
9 Ø. B. Vistad, E. W. Hansen, D. E. Akporiaye and K. P. Lillerud, *J. Phys. Chem. A*, 1999, **103**, 2540–2552.
10 Z. M. Yan, B. H. Chen and Y. Huang, *Solid State Nucl. Magn. Reson.*, 2009, **35**, 49–60.
11 G. J. Yang, Y. X. Wei, S. T. Xu, J. R. Chen, J. Z. Li, Z. M. Li, J. H. Yu and R. R. Xu, *J. Phys. Chem. C*, 2013, **117**, 8214–8222.
12 L. Zhang, J. Bates, D. H. Chen, H. Y. Nie and Y. N. Huang, *J. Phys. Chem. C*, 2011, **115**, 22309–22319.
13 H. Koningsveld, Schemes for Building Zeolite Framework Models, http://www.iza-structure.org/databases/, accessed February 26, 2014.
14 L. Leardini, S. Quartieri and G. Vezzalini, *Microporous Mesoporous Mater.*, 2010, **127**, 219–227.
15 J. Z. Li, Y. X. Wei, J. R. Chen, P. Tian, X. Su, S. T. Xu, Y. Qi, Q. Y. Wang, Y. Zhou, Y. L. He and Z. M. Liu, *J. Am. Chem. Soc.*, 2012, **134**, 836–839.

16 W. G. Song, H. Fu and J. F. Haw, *J. Am. Chem. Soc.*, 2001, **123**, 4749–4754.
17 W. G. Song, H. Fu and J. F. Haw, *J. Phys. Chem. B*, 2001, **105**, 12839–12843.
18 W. G. Song, J. F. Haw, J. B. Nicholas and C. S. Heneghan, *J. Am. Chem. Soc.*, 2000, **122**, 10726–10727.
19 S. Wilson and P. Barger, *Microporous Mesoporous Mater.*, 1999, **29**, 117–126.
20 U. Olsbye, S. Svelle, M. Bjørgen, P. Beato, T. V. W. Janssens, F. Joensen, S. Bordiga and K. P. Lillerud, *Angew. Chem., Int. Ed.*, 2012, **51**, 5810–5831.
21 G. Y. Liu, P. Tian, Y. Zhang, J. Z. Li, L. Xu, S. H. Meng and Z. M. Liu, *Microporous Mesoporous Mater.*, 2008, **114**, 416–423.
22 D. Fan, P. Tian, S. T. Xu, Q. H. Xia, X. Su, L. Zhang, Y. Zhang, Y. L. He and Z. M. Liu, *J. Mater. Chem.*, 2012, **22**, 6568–6574.
23 N. A. Khan, J. H. Park and S. H. Jhung, *Mater. Res. Bull.*, 2010, **45**, 377–381.
24 Y. Jin, Q. Sun, G. Qi, C. Yang, J. Xu, F. Chen, X. Meng, F. Deng and F.-S. Xiao, *Angew. Chem., Int. Ed.*, 2013, **52**, 9172–9175.
25 M. Elanany, B.-L. Su and D. P. Vercauteren, *J. Mol. Catal. A: Chem.*, 2007, **270**, 295–301.
26 M. Briend, R. Vomscheid, M. J. Peltre, P. P. Man and D. Barthomeuf, *J. Phys. Chem.*, 1995, **99**, 8270–8276.
27 N. Nishiyama, M. Kawaguchi, Y. Hirota, D. Van Vu, Y. Egashira and K. Ueyama, *Appl. Catal., A*, 2009, **362**, 193–199.
28 R. Vomscheid, M. Briend, M. J. Peltre, P. P. Man and D. Barthomeuf, *J. Phys. Chem.*, 1994, **98**, 9614–9618.
29 E. Dumitriu, A. Azzouz, V. Hulea, D. Lutic and H. Kessler, *Microporous Mater.*, 1997, **10**, 1–12.
30 G. Liu, P. Tian, J. Li, D. Zhang, F. Zhou and Z. Liu, *Microporous Mesoporous Mater.*, 2008, **111**, 143–149.
31 A. M. Prakash and S. Unnikrishnan, *J. Chem. Soc., Faraday Trans.*, 1994, **90**, 2291–2296.
32 N. Rajic, D. Stojakovic, S. Hocevar and V. Kaucic, *Zeolites*, 1993, **13**, 384–387.
33 B. Han, C. H. Shin, P. A. Cox and S. B. Hong, *J. Phys. Chem. B*, 2006, **110**, 8188–8193.
34 G. Mali, A. Meden, A. Ristic, N. N. Tusar and V. Kaucic, *J. Phys. Chem. B*, 2002, **106**, 63–69.
35 D. Fan, P. Tian, X. Su, Y. Y. Yuan, D. H. Wang, C. Wang, M. Yang, L. Y. Wang, S. T. Xu and Z. M. Liu, *J. Mater. Chem. A*, 2013, **1**, 14206–14213.
36 D. W. Lewis, C. M. Freeman and C. R. A. Catlow, *J. Phys. Chem.*, 1995, **99**, 11194–11202.
37 J. Li, J. Yu and R. Xu, *Microporous Mesoporous Mater.*, 2007, **101**, 406–412.
38 Y. Song, J. Y. Li, J. H. Yu, K. X. Wang and R. R. Xu, *Top. Catal.*, 2005, **35**, 3–8.
39 D. W. Lewis, D. J. Willock, C. R. A. Catlow, J. M. Thomas and G. J. Hutchings, *Nature*, 1996, **382**, 604–606.
40 L. Gomez-Hortiguela, F. Lopez-Arbeloa, F. Cora and J. Perez-Pariente, *J. Am. Chem. Soc.*, 2008, **130**, 13274–13284.
41 T. Yamaji, T. Saito, K. Hayamizu, M. Yanagisawa and O. Yamamoto, Spectral Database for Organic Compounds, SDBS, http://sdbs.db.aist.go.jp/sdbs/cgi-bin/cre_index.cgi, accessed February 26, 2014, 2014.
42 L. Gomez-Hortiguela, J. Perez-Pariente, F. Cora, C. R. A. Catlow and T. Blasco, *J. Phys. Chem. B*, 2005, **109**, 21539–21548.
43 A. Burton, S. Elomari, C.-Y. Chen, R. C. Medrud, I. Y. Chan, L. M. Bull, C. Kibby, T. V. Harris, S. I. Zones and E. S. Vittoratos, *Chem. – Eur. J.*, 2003, **9**, 5737–5748.
44 L. Gomez-Hortiguela, S. Hamad, F. Lopez-Arbeloa, A. B. Pinar, J. Perez-Pariente and F. Cora, *J. Am. Chem. Soc.*, 2009, **131**, 16509–16524.
45 L. Gomez-Hortiguela, A. B. Pinar, J. Perez-Pariente and F. Cora, *Chem. Mater.*, 2009, **21**, 3447–3457.
46 H. Sun, S. J. Mumby, J. R. Maple and A. T. Hagler, *J. Phys. Chem.*, 1995, **99**, 5873–5882.
47 M. Zokaie, D. S. Wragg, A. Gronvold, T. Fuglerud, J. H. Cavka, K. P. Lillerud and O. Swang, *Microporous Mesoporous Mater.*, 2013, **165**, 1–5.
48 J. Li, L. Li, J. Liang, P. Chen, J. Yu, Y. Xu and R. Xu, *Cryst. Growth Des.*, 2008, **8**, 2318–2323.
49 P. Tian, B. Li, S. Xu, X. Su, D. Wang, L. Zhang, D. Fan, Y. Qi and Z. Liu, *J. Phys. Chem. C*, 2013, **117**, 4048–4056.
50 L.-T. Yuen, S. I. Zones, T. V. Harris, E. J. Gallegos and A. Auroux, *Microporous Mater.*, 1994, **2**, 105–117.
51 D. Mores, E. Stavitski, M. H. F. Kox, J. Kornatowski, U. Olsbye and B. M. Weckhuysen, *Chem. – Eur. J.*, 2008, **14**, 11320–11327.

